Pythagoras superposition principle for localized eigenstates of two-dimensional moiré lattices

Zixuan Gao, Zhenli Xu, and Zhiguo Yang
School of Mathematical Sciences, CMA-Shanghai, MOE-LSC and Shanghai Center for Applied Mathematics, Shanghai Jiao Tong University, Shanghai 200240, People's Republic of China

Fangwei Ye
School of Physics and Astronomy, Shanghai Jiao Tong University, Shanghai 200240, People's Republic of China

(Received 18 November 2022; revised 30 June 2023; accepted 10 July 2023; published 21 July 2023)

Moiré lattices are aperiodic systems formed by a superposition of two periodic lattices with a relative rotational angle. In optics, the photonic moiré lattice has many appealing properties such as its ability to localize light, thus attracting much attention on exploring features of such a structure. One fundamental research area for photonic moiré lattices is the properties of eigenstates, particularly the existence of localized eigenstates and the localization-to-delocalization transition in the energy band structure. Here we propose an accurate algorithm for the eigenproblems of aperiodic systems by combining plane-wave discretization and spectral indicator validation under the higher-dimensional projection, allowing us to explore energy bands of fully aperiodic systems. A localization-delocalization transition regarding the intensity of the aperiodic potential is observed and a Pythagoras superposition principle for localized eigenstates of two-dimensional moiré lattices is revealed by analyzing the relationship between the aperiodic system and its corresponding periodic eigenstates. This principle sheds light on exploring the physics of localizations for moiré lattices.

DOI: 10.1103/PhysRevA.108.013513

I. INTRODUCTION

The structural geometrical properties of natural or artificial systems profoundly impact the properties of waves that are allowed to propagate in them. Thus, a fascinating range of phenomena stemming from the geometrical properties of material landscapes, such as their periodicity, are continuously discovered in diverse areas of physics, including mechanics, acoustics, optics, electronics, solid-state physics, and physics of matter waves [1–10]. Recently, moiré systems [11–16] have drawn much attention due to their unusual electronic, optical, and magnetic properties, and their potential for designing novel materials with tailored functionalities [17,18]. A moiré system is a system that involves two or more periodic structures with different lattice constants or orientation, which interact with each other to form a spatial moiré pattern. These systems can arise in a variety of fields such as materials science, condensed-matter physics, optics, and electronics. For example, in condensed-matter physics, the moiré systems are revealing a wealth of profound physical effects that have established a new area of research referred to as twistronics [3]. Moiré patterns are also crucial in all areas of physics related to wave propagation, such as Bose-Einstein condensates and optics [8,9], where they afford the possibility to explore the phenomena that arise because of the transition from aperiodic (incommensurate) to periodic (commensurate) geometries, occurring at specific values of the rotation angle in contrast to aperiodic quasicrystal systems.

Photonic moiré lattices can be created by the superposition of two rotated square or hexagonal sublattices [19,20]. Recent experiments have reported the observation of the two-dimensional (2D) localization-delocalization transition (LDT) [19] of light waves when one tunes the twisting angles or the depth of the modulation of the constitute sublattices. In one dimension, the LDT effect has been observed for both light [21] and matter waves [22]. The localization phenomenon is due to the band flattening of the moiré pattern in the incommensurate (namely, aperiodic) phase [19]. Theoretically, the properties of localized eigenstates and the existence of the LDT in the eigenvalue spectrum for a fixed moiré lattice remain less explored due to the difficulty in calculating eigenproblems for aperiodic systems. Traditional crystalline approximant methods [23,24] are slowly convergent and cannot provide results accurate enough for physical understanding. In this article, we develop an efficient method to solve the aperiodic problems, which allows us to explore the properties of localized eigenstates in moiré lattices, and by this method we reveal the Pythagoras superposition principle between the aperiodic system and its periodic crystalline approximants.

In the paraxial approximation, the propagation of an extraordinarily polarized beam in a photorefractive medium with an optically induced refractive index is described by the Schrödinger-like equation of the dimensionless field amplitude $\phi(\boldsymbol{r}, z)$ [25]:

$$i\frac{\partial \phi}{\partial z} = -\frac{1}{2}\nabla^2\phi + \frac{E_0}{1+I(\boldsymbol{r})}\phi, \tag{1}$$

where $\boldsymbol{r} = (x, y)$ and $I(\boldsymbol{r}) = |p_1 v(\boldsymbol{r}) + p_2 v(S\boldsymbol{r})|^2$ is the intensity of the moiré lattice induced by two ordinarily polarized mutually coherent periodic sublattices, $v(\boldsymbol{r})$ and $v(S\boldsymbol{r})$. Here S is a 2D rotational matrix such that $S(\theta)\boldsymbol{r}$ rotates vector $\boldsymbol{r}$ by a counterclockwise angle θ. p_1 and p_2 are the amplitudes of the

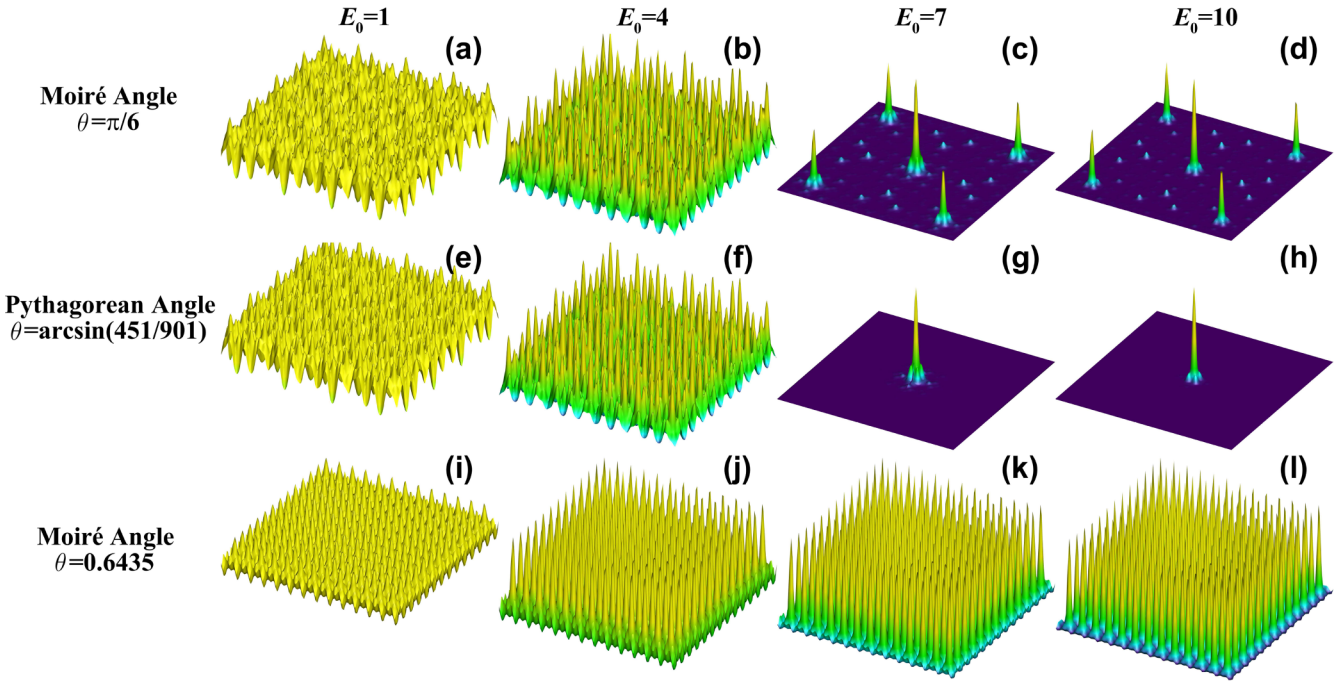

FIG. 1. The first eigenstates $|\psi|^2$ of the lattices for $E_0 = 1, 4, 7$, and 10 with twist angles: (a–d) $\theta = \pi/6$, (e–h) $\theta = \arcsin(451/901)$, and (i–l) $\theta = 0.6435$. Here the $\theta = \arcsin(451/901)$ cases correspond to a periodic system whose twist angle approximates $\pi/6$.

first and second sublattices, and p_1/p_2 is defined as the lattice ratio. The potential term $V(\boldsymbol{r}) = E_0/[1 + I(\boldsymbol{r})]$ describes the optical response of the photorefractive crystal [19,20], where E_0 describes the strength. Notably, the moiré structures can be periodic or aperiodic, depending on the twisting angle θ. The moiré lattices composed of two square lattices, as considered here, are periodic when θ takes any Pythagorean angle and aperiodic otherwise [20]. Throughout this article, the sublattices of the moiré systems have the fixed parameter $p_1/p_2 = 1$.

To visualize the mysterious properties of moiré lattices, Fig. 1 presents the first eigenstates of aperiodic systems for different E_0 with $\theta = \pi/6$ and periodic crystalline approximants with Pythagorean angle $\theta = \arcsin(451/901)$ which approximates $\pi/6$ with the error $\sim 2 \times 10^{-4}\pi$, together with the results of aperiodic systems with $\theta = 0.6435$ which approximates the Pythagorean angle $\arcsin(3/5)$. These data describe the results in the domain $[-33.3401, 33.3401]^2$. Here the aperiodic systems are calculated by the projection indicator (PI) method described below, while the periodic systems are solved by the plane-wave method [26]. The photonic lattice actually acts as an effective potential that can trap or diffuse light during its propagation and the larger modulus indicates a stronger effective potential. These results clearly show a more localized tendency with the increase of E_0. At $E_0 = 7$ and 10, both the aperiodic and periodic systems demonstrate mode localization. We note that, although the lattice for Figs. 1(e)–(h) is periodic, the width of the wave packet in $E_0 = 7$ and $\theta = \arcsin(451/901)$ is 2.813, which is much less than the period $T = \sqrt{901/2}\pi$, implying that the eigenstate of the periodic approximant is localized. This localized eigenstate shows that a localized light field having the central ring shape in the transverse plane is obtained, indicating a localized high-order light mode [27]. Oppositely, for $\theta = 0.6435$, which is close to the Pythagorean angle $\arcsin(3/5)$, the eigenstates are delocalized since the $\theta = 0.6435$ system can be approximated by a periodic system with a much smaller period of $T = \sqrt{5/2}\pi$.

Interestingly, the eigenstate of the aperiodic systems features a lot of sharp peaks and looks completely different from that of its periodic companion, comparing between $\theta = \pi/6$ and $\arcsin(451/901)$. Different from the nonlocalized light fields, peaks of the localized moiré light field are more like a superposition of several ring-shape localized light fields rather than side lobes around the central main lobes, indicating a weakly diffusing effect [27]. Each peak corresponds to a localized light field in the neighborhood and the photonic moiré lattices have some ability to trap the light during its propagation. This is counterintuitive, taking into account that the difference in rotation angles of two systems is negligible, illustrating the discontinuity in eigenstates with the rotation angle. Thus, generally, this tells the breakdown of the traditional crystalline approximant method [23,24] to solve the eigenstates of the aperiodic systems and the error cannot be controlled due to the simultaneous Diophantine approximation [28]. Another commonly employed approach for addressing similar problems is the continuum model Hamiltonian method [1]. This method solves the Hamiltonian structure [14] of the moiré system in the specific area. Instead of truncating the traditional domain in physical space, the continuum model Hamiltonian method truncates the momentum-space lattice at the first shell, thereby rendering a truncation error of momentum space similar to that of the conventional crystalline approximant method. This motivates us to propose an efficient and accurate method for aperiodic eigenvalue problems

that circumvents the error like simultaneous Diophantine error.

II. METHOD

Here we develop the projection indicator (PI) method to solve the eigenproblem of the Schrödinger equation

$$E\psi = -\frac{1}{2}\nabla^2\psi + \frac{E_0}{1+I(\boldsymbol{r})}\psi, \tag{2}$$

by a combination of the projection method [29] and the indicator projection with plane-wave discretizations. For simplicity, one chooses the projection matrix $\boldsymbol{P}$ so that the period in each direction is 2π, expressed as

$$\boldsymbol{P} = 2\begin{bmatrix} \cos\gamma & -\sin\gamma & \cos\gamma & \sin\gamma \\ \sin\gamma & \cos\gamma & -\sin\gamma & \cos\gamma \end{bmatrix}, \tag{3}$$

with $\gamma = \theta/2$, where the projection direction is in parallel to the shortest periodic edge of the 4D periodic system. By the projection matrix $\boldsymbol{P}$, one can obtain the transition from 2D to 4D spaces, $\boldsymbol{q} = \boldsymbol{P}^\top \boldsymbol{r}$, with $\boldsymbol{q} = (q_1, q_2, q_3, q_4)$. Then substituting $\phi = e^{-iEt}\psi$ into Eq. (1) leads to a 4D eigenproblem,

$$E\psi = -\frac{1}{2}\sum_{i,j=1}^{4}\frac{\partial^2\psi}{\partial q_i \partial q_j}\left(\frac{\partial q_i}{\partial x}\frac{\partial q_j}{\partial x} + \frac{\partial q_i}{\partial y}\frac{\partial q_j}{\partial y}\right) + \tilde{V}(\boldsymbol{q})\psi. \tag{4}$$

Here $\tilde{V}(\boldsymbol{q})$ represents the potential function $V(\boldsymbol{r})$ after being lifted to a 4D space, which implies that, if $\boldsymbol{q} = \boldsymbol{P}^\top\boldsymbol{r}$ holds, then $\tilde{V}(\boldsymbol{q}) = V(\boldsymbol{r})$. $\tilde{V}(\boldsymbol{q})$ is a periodic function with the period $[0, 2\pi]^4$, and thus Eq. (4) is a 4D periodic eigenproblem. The numerical solution $\tilde{\psi}_N$ of Eq. (4) can be expanded using the plane-wave expansion as

$$\tilde{\psi}_N(\boldsymbol{q}) = \sum_{\boldsymbol{k}\in\Omega}\psi_{\boldsymbol{k}} e^{i\langle \boldsymbol{k},\boldsymbol{q}\rangle}. \tag{5}$$

Here $\langle\cdot,\cdot\rangle$ denotes the standard inner product between vectors, $\Omega = \mathbb{Z}^4 \cap \{||\boldsymbol{k}||_\infty \leqslant N\}$ is the basis space, and N represents the number of spectral modes in each dimension, and $\psi_{\boldsymbol{k}}$ are the Fourier expansion coefficients. Let $\boldsymbol{k} = (k_1, \ldots, k_4)$. Equation (4) can be transformed into

$$E\psi_{\boldsymbol{k}} = \frac{1}{2}\sum_{i=1}^{2}\sum_{j=1}^{4}\sum_{l=1}^{4}\left(\psi_{\boldsymbol{k}} k_j k_l \frac{\partial q_j}{\partial r_i}\frac{\partial q_l}{\partial r_i}\right) + \mathcal{F}\{V\psi\}_{\boldsymbol{k}}, \tag{6}$$

where $\mathcal{F}\{\cdot\}$ denotes the Fourier transform and $\mathcal{F}\{V\psi\}_{\boldsymbol{k}}$ is the Fourier coefficient of $\mathcal{F}\{V\psi\}$ with the frequency $\boldsymbol{k}$. Set a column vector $\vec{\psi}$ containing all the Fourier expansion coefficients $\psi_{\boldsymbol{k}}$. Hence, one can form a matrix $\boldsymbol{A}$ to transform Eq. (6) into the matrix eigenproblem $\boldsymbol{A}\vec{\psi} = E\vec{\psi}$. Due to the enormous size of $\boldsymbol{A}$, which is not sparse, it cannot be stored explicitly. Therefore, we use a matrix-free preconditioned Krylov subspace method [30] which only requires the matrix-vector product to be stored in each iteration, making it a more efficient approach. Once the eigenvector $\vec{\psi}$ is obtained, the four-dimensional eigenfunction $\psi(\boldsymbol{q})$ can be approximated using Eq. (5). By the projection matrix $\boldsymbol{P}$, $\tilde{\psi}_N$ can be transformed back to the 2D space, which implies that

$$\tilde{\psi}_N(\boldsymbol{q}) = \sum_{\boldsymbol{k}\in\Omega}\psi_{\boldsymbol{k}} e^{i\langle \boldsymbol{k},\boldsymbol{q}\rangle} = \sum_{\boldsymbol{k}\in\Omega}\psi_{\boldsymbol{k}} e^{i\langle \boldsymbol{P}\boldsymbol{k},\boldsymbol{r}\rangle} := \psi_N(\boldsymbol{r}). \tag{7}$$

Here the second equality uses $\langle \boldsymbol{k}, \boldsymbol{P}^\top\boldsymbol{r}\rangle = \langle \boldsymbol{P}\boldsymbol{k}, \boldsymbol{r}\rangle$. The 2D aperiodic function $\psi_N(\boldsymbol{r})$ as the eigenfunction and E as the eigenvalue are the numerical results of the original problem, Eq. (1), returned by the PI. Therefore, this approach is equivalent to solving the higher-dimensional periodic lattice problem within the subspace of the original problem, applying the plane-wave method. On the other hand, if the twisting angle is such that the moiré lattices restore periodicity, one can solve the corresponding eigenproblem directly in the original (2D) space, using the plane-wave method, thanks to the Floquet-Bloch theorem [31].

Due to the singularity of the eigenvalue problem, especially when E_0 is large, the error in the numerical calculation may lead to some spurious eigenstates. In order to sift out pseudo-eigenstates, a spectral indicator method [32–34] is adopted. Define the indicator [35] as

$$\mathrm{Ind} = \|\boldsymbol{Q}(\boldsymbol{Q}\boldsymbol{f}/\|\boldsymbol{Q}\boldsymbol{f}\|)\|, \tag{8}$$

where matrix $\boldsymbol{Q}$ is the spectral projection,

$$\boldsymbol{Q} = \frac{1}{2\pi i}\int_\Gamma (\boldsymbol{A} - s\boldsymbol{I})^{-1} ds, \tag{9}$$

with $\boldsymbol{I}$ being the identity matrix. The indicator becomes 1 if there exists at least one eigenvalue in the square. To evaluate the integral, the closed path is divided uniformly into four parts and the composite trapezoidal rule is employed to compute $\boldsymbol{Q}\boldsymbol{f}$, where $\boldsymbol{f}$ takes the potential function V directly. The numerical approximation of $\boldsymbol{Q}\boldsymbol{f}$ can be obtained via a certain quadrature rule:

$$\boldsymbol{Q}\boldsymbol{f} \approx \frac{1}{2\pi i}\sum_{j=1}^{n_0}\omega_j \boldsymbol{r}_j. \tag{10}$$

Here $\{\omega_j\}$ are quadrature weights and $\{\boldsymbol{r}_j\}$ are the solutions of the linear systems

$$(\boldsymbol{A} - s_j\boldsymbol{I})\boldsymbol{r}_j = \boldsymbol{f}, \;\; j = 1, 2, \ldots, n_0, \tag{11}$$

where $\{s_j\}$ are the quadrature nodes on Γ. For simplicity, the piecewise trapezoid formula is chosen for the curve integral, Eq. (9). The size of Γ is small such that only a few sample points guarantee high accuracy. Since the spectral projection method provides many solutions of Eq. (4), we can take a small domain around each eigenvalue and calculate the indicator value to validate the correctness of this eigenvalue. Detailed steps of the PI are included in Algorithm 1.

III. ACCURACY PERFORMANCE

To validate the accuracy performance of the PI method, the absolute errors of the first eigenvalues are evaluated and displayed in Fig. 2 where panels (a) and (b) correspond to 1D and 2D moiré systems, respectively. Here the 1D moiré system is with the potential $V(x) = E_0/[1 + I(x)]$ for $I(x) = [\cos(2x\cos\theta) + \cos(2x\sin\theta)]^2$, and the rotation angle is set as $\pi/6$. The results for three cases of $E_0 = 1$, $3/2$, and 7 are presented with the increase of N. In the low-strength cases $E_0 = 1$ and $3/2$, the eigenstates are delocalized and one can see the spectral convergence of the numerical approximation. Conversely, in the strong-strength case $E_0 = 7$, the numerical approximation converges slower and more nodes are needed

Algorithm 1 Projection indicator method.

Data: d-dimensional aperiodic potential V, the number of bases N in each dimension, the number of eigenvalues M, the step size δ, and the threshold value ϵ
1 Determine the basis space and the test space Ω
2 Compute the first M eigenpairs of $\boldsymbol{A}$ as $\{(E_m, u_m)\}_{m=1}^{M}$
3 **for** $m = 1$ to M **do**
4 Set $\omega = [E_m - \delta/2, E_m + \delta/2]^2$ and $\boldsymbol{f}$ by V
5 Compute the indicator $\mathrm{Ind} = \|\boldsymbol{Q}(\boldsymbol{Qf}/\|\boldsymbol{Qf}\|)\|$ by Eq. (9)
6 if $\mathrm{Ind} < \epsilon$ **then**
7 Delete the eigenpair (E_m, u_m)
8 **end**
9 Project the eigenfunctions u_m back into the d-dimensional space
10 **end**

to achieve high accuracy. These results demonstrate that the larger E_0 is, the more singular the system is, and the slower the convergence of numerical results is. In 1D, a small value of N can achieve an accuracy of approximately 10^{-10} for $E_0 = 1$. For 2D systems, rapid convergences are observed for both cases of $E_0 = 1$ and $E_0 = 3/2$. These results demonstrate the high accuracy and the fast convergence of the PI method for low-strength cases.

For systems with large strength E_0, the eigenfunctions tend to be localized. This makes numerical calculation more challenging to achieve high accuracy. Consequently, if the numerical error in the eigenfunction is significant, the wave function of the time evolution will be unable to remain unchanged during the propagation. By examining the wave propagation behavior by the time-dependent Schrödinger equation, Eq. (1), one can validate the accuracy of the eigenstates obtained through the PI. Figure 3 presents the results of the 1D moiré system at different times. The initial condition takes the eigenfunctions for $E_0 = 4$ and 7, which are calculated using the PI with $N = 50$. One can observe that for the case of $E_0 = 7$ the wave function remains unaltered regardless of the propagation time. However, for a smaller strength of $E_0 = 4$, the wave function exhibits slight oscillation changes during propagation. The behavior shows the stable propagation of the localized eigenstate and the results demonstrate that the PI method provides an accurate solution even when the eigenfunctions are localized.

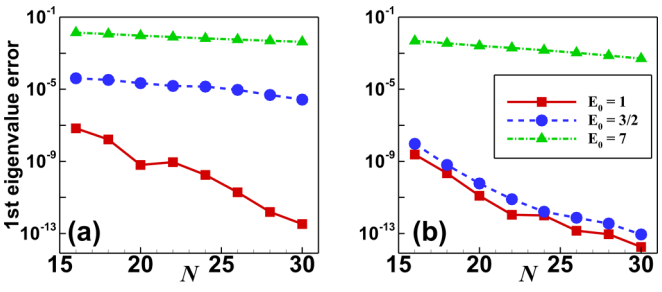

FIG. 2. Error of the first eigenvalue of moiré systems with the increase of N for $E_0 = 1$, 3/2, and 7. (a) The 1D case. (b) The 2D case.

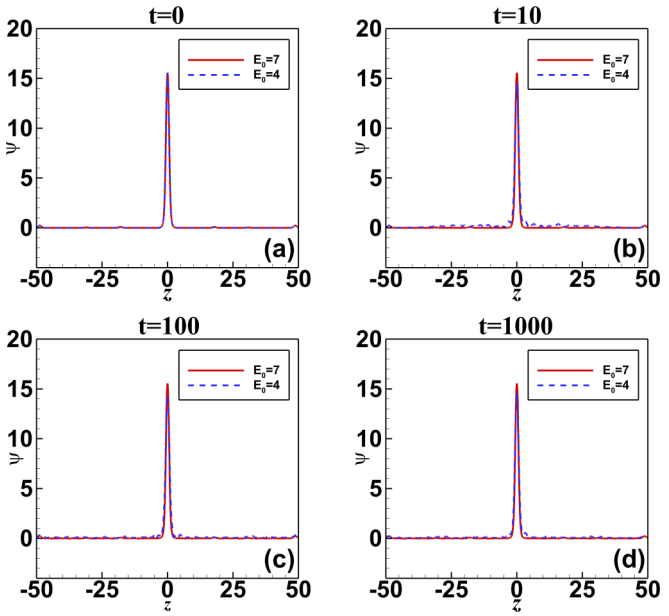

FIG. 3. Wave propagation of 1D aperiodic potentials at $E_0 = 4$ and 7. Panels (a)–(d) correspond to the results at time $t = 0$, 10, 100, and 1000.

To further validate the accuracy of the PI for localized eigenstates, we calculate the first six eigenvalues of the 2D aperiodic systems with $E_0 = 4$ and 7 and display the results in Fig. 4. In the spectral projection step, 24 and 32 spectral nodes are used in each dimension, and the spectral indicator sets the size of Γ to be 2.5×10^{-4}. Notably, the overall errors are less than 10^{-3}, serving as evidence of the high accuracy of the PI. The indicator-only method is used to verify the accuracy of the PI results, which involves searching for eigenvalues across the entire domain. For the results obtained through the spectral projection step, one finds that less than half of the eigenvalues are validated by the indicator method. This highlights the necessity of the indicator test in ensuring accuracy.

IV. PYTHAGORAS SUPERPOSITION PRINCIPLE

We are now ready to study the energy bands and the LDT phenomenon of 2D photonic moiré lattices. The LDT in moiré

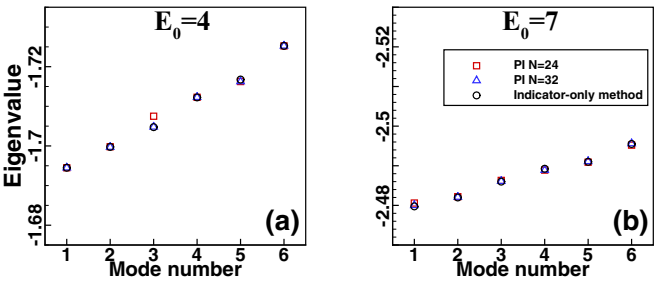

FIG. 4. The eigenvalues obtained by the PI method and the indicator-only method. The first six eigenvalues of 2D aperiodic systems with $E_0 = 4$ and 7 are displayed. The projection method uses plane waves $N = 24$ and 32 along one direction. The indicator method uses intervals of size 2.5×10^{-4}.

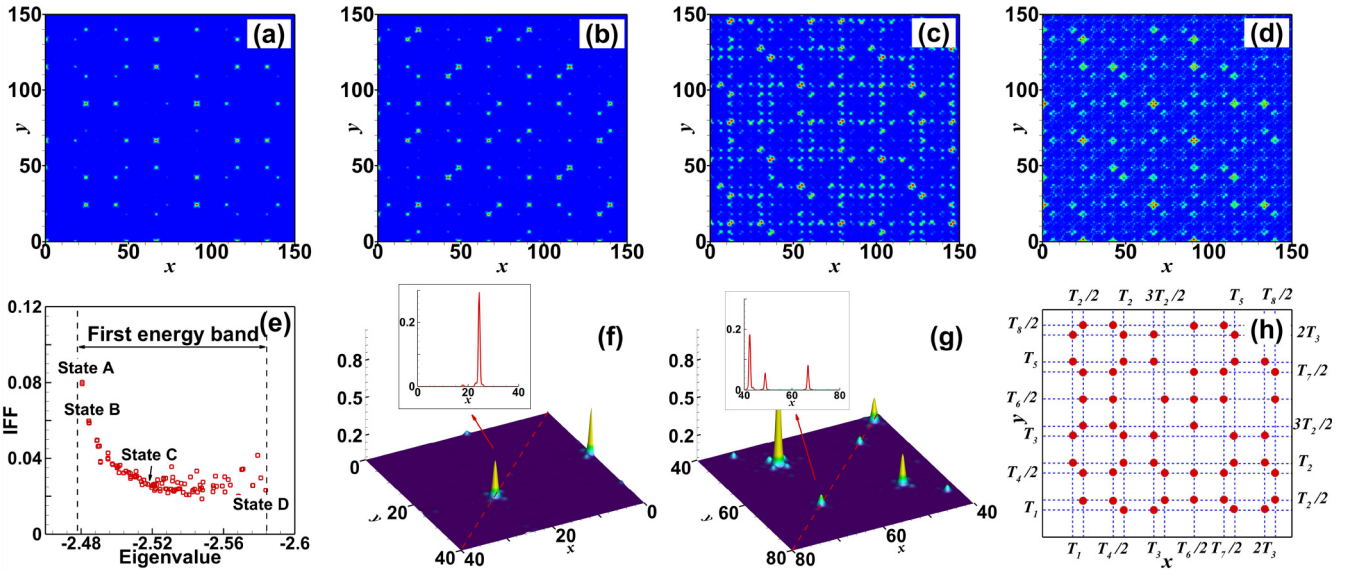

FIG. 5. Results of the 2D aperiodic system at $E_0 = 7$ and $\theta = \pi/6$. (a, b) Contours of the first and third eigenstates. (c, d) Contours of the eigenstates at the middle (41st) and the bottom (109th) of the first energy band. (e) The IFFs of all the eigenstates in the first energy band as a function of eigenvalue. States A–D correspond to the eigenstates of panels (a)–(d). (f, g) Enlarged plots of the first eigenstate in two domains, $[0, 40]^2$ and $[40, 80]^2$, with the $y = x$ cuts. (h) The peak sites of interior wave packets (red circles) in panel (a), which are located at the nodes of the T mesh.

lattice with respect to the change of the lattice ratio was discussed in Wang *et al.* [19]. However, the effect of varying E_0 on localization remains unclear. The PI method is used to calculate the eigenstates of the moiré system. Through the location of the peaks in the localized eigenstates, one can deduce the localization position of the wave packets propagated in this system. Here we consider the 2D aperiodic systems at $E_0 = 7$ and $\theta = \pi/6$ and attempt to understand the misconvergence of the simultaneous Diophantine approximation. Figures 5(a)–5(d) show the 1st, 3rd, 41st, and 109th eigenstates for $|\psi|^2$, with $N = 30$. The two eigenstates of Figs. 5(c) and 5(d) are at the middle and the bottom of the first energy band of the aperiodic system, where the degree of localization decreases with the increase of mode numbers. A quantitative description of the localization degree of the eigenstates in a given region U is the integral form factor (IFF) [19,36] expressed by

$$\mathrm{IFF} = \frac{\left(\int_U |\psi|^4 d^2\boldsymbol{r}\right)^{1/2}}{\int_U |\psi|^2 d^2\boldsymbol{r}}. \tag{12}$$

A larger IFF means a more localized state of the eigenfunction ψ. Figure 5(e) displays the IFFs of all eigenstates in the first energy band, where states A–D correspond to Figs. 5(a)–5(d), respectively. One observes the decreasing tendency of the IFF value with the mode index.

The first eigenstate of the aperiodic system is the only one with an IFF bigger than 0.05. In order to verify the localization character, the enlarged plots of the eigenstate are present in Figs. 5(f) and 5(g), together with the $y = x$ cuts for $|\psi|^2$. The exponential decay of the wave packets can be observed, demonstrating the exponential localization characteristics of the eigenfunction. Figures 5(a)–5(d) thus verify the mode transition from localization into delocalization with the increasing of the mode index in the energy spectrum. This is in agreement with the experimental demonstration [19] of the LDT in 2D photonic moiré lattices, which revealed the mechanics for wave localization based on flat-band structure, in contrast to the schemes based on light diffusion in photonic quasicrystals requiring disorder media [37,38].

The difference between aperiodic eigenstates and their periodic approximants can be also illustrated by the phase structures of the first eigenstates. Figure 6 displays the results of the localized system with parameters $E_0 = 7$ and $\theta = \pi/6$ and its periodic approximant. For localized systems, Fig. 6(a) depicts that the phase does not change very frequently with space. In some areas, there also exist abrupt changes in phase, which implies that the moiré lattice can also preserve the topological phase structure of the localized light mode. While in Fig. 6(b), the phase of periodic approximants changes periodically and strongly. These differences show that direct periodic approximation may not preserve physical properties well.

Moreover, Fig. 1 has indicated that the crystalline approximants do not converge to the aperiodic system. Consequently,

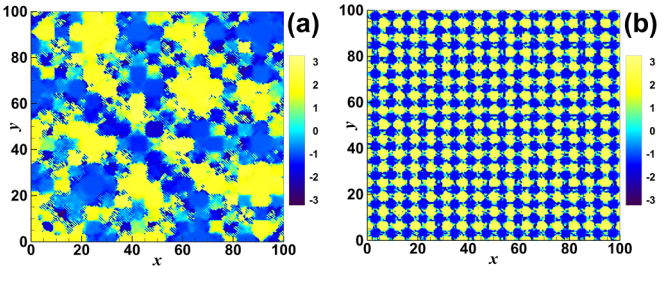

FIG. 6. The phase structure of the first eigenstate of the PI. (a) The aperiodic localized system. (b) The periodic approximant.

TABLE I. Parameters of nine periodic systems near $\pi/6$.

c	θ	T
65	$0.169\,500\pi$	$T_1 = \sqrt{65/2}\pi$
241	$0.165\,903\pi$	$T_2 = \sqrt{241}\pi$
901	$0.166\,858\pi$	$T_3 = \sqrt{901/2}\pi$
725	$0.167\,431\pi$	$T_4 = \sqrt{725}\pi$
2701	$0.166\,476\pi$	$T_5 = \sqrt{2701/2}\pi$
3361	$0.166\,603\pi$	$T_6 = \sqrt{3361}\pi$
4813	$0.167\,081\pi$	$T_7 = \sqrt{4813}\pi$
7925	$0.163\,487\pi$	$T_8 = \sqrt{7925}\pi$
10 085	$0.166\,731\pi$	$T_9 = \sqrt{10\,085}\pi$

the IFFs of the aperiodic system are significantly smaller than the results of its periodic counterpart. In order to connect the relations between the moiré lattice and its crystalline approximants, we introduce a Pythagoras triple (a, b, c) to represent a Pythagoras angle such that $\sin\theta = a/c$. Let the central cell be $[0, T]^2$, where $T = \sqrt{c}\pi$ or $\sqrt{c/2}\pi$ is the period. Due to the symmetry of the potential, the first eigenfunction is composed of wave packets located at the four corners of the cell for the period $\sqrt{c/2}\pi$, or of wave packets at the corners and the center of the cell for the period $\sqrt{c}\pi$. Table I lists the c, θ, and T values of the nine periodic approximants to the moiré angle (with the period $T_i < 150$, $i = 1, \ldots, 9$). Figure 5(h) displays that the peak sites of those interior wave packets are all located at the nodes of the T mesh (grid points $nT_i/2$ for integer n) for the first eigenstate shown in Fig. 5(a). One can clearly observe that these happen to be the packet sites by all these periodic approximants. This counterpart clearly appears as a superposition principle for localized eigenstates of the Pythagoras angles. This is to say that an eigenstate of the moiré lattice can be considered as the summation of the eigenstates of its crystalline approximants, and the weight of each approximant depends on the Diophantine error between the twist angles. The periodic systems near $\theta = \pi/6$ have large periods, while the periodic system with the smallest period, $\theta = \arcsin(3/5)$, is near $\theta = 0.6435$. By the superposition principle, when E_0 is large the eigenstates of the former systems show sparse peak distribution, while the peaks of the eigenstates of $\theta = 0.6435$ are very dense. This conclusion is consistent with the numerical results in Fig. 1.

To provide a theoretical understanding of the Pythagoras superposition principle, we consider the simplified 1D aperiodic system whose equation is Eq. (2). Here the use of the 1D system is due to its intuitive physical picture and the corresponding Schrödinger-like equation is also easy to solve in the incremental space (q_1, q_2). Figures 7(a)–7(c) show the contour of the first eigenstates of different rotation angles $\pi/6$, $\pi/4$, and $\pi/8$ in the $\boldsymbol{q}$ space, where some localized regions of javelin shape can be observed, and we denote them as the localization in higher dimensions. The projection lines defined by $q_2 = \tan(\pi/12)q_1$, $q_2 = \tan(\pi/4)q_1$, and $q_2 = \tan(\pi/16)q_1$ describe the physical solutions of the aperiodic systems. Since each projection line is not parallel to the javelin-shaped domain, it intersects with many domains, leading to the wave packets of the physical space in a lower dimension. The localization phenomenon is independent of the rotation angle. Figure 7(d) shows these packets

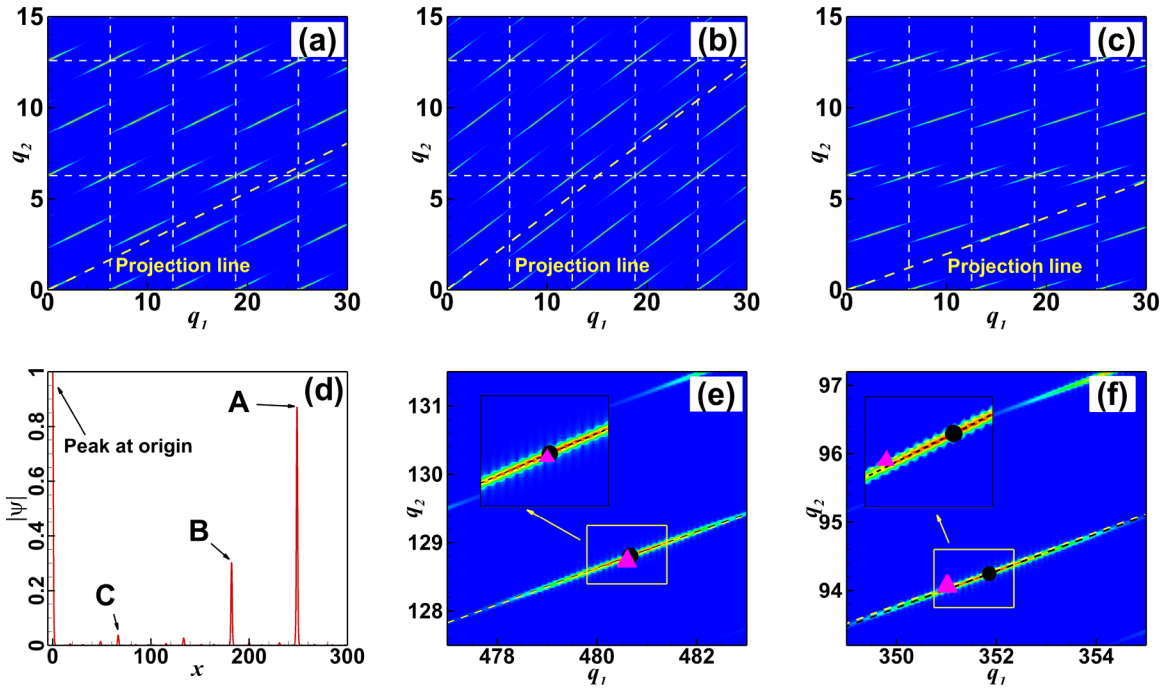

FIG. 7. The first eigenstate of the 1D aperiodic system. (a–c) The contour plots in the incremental space of the rotation angles $\pi/6$, $\pi/4$, and $\pi/8$, respectively. The corresponding projection lines are $q_2 = \tan(\pi/12)q_1$, $q_2 = \tan(\pi/4)q_1$, and $q_2 = \tan(\pi/16)q_1$, respectively. (d) The projected eigenstate in the physical space and the widths of peaks A–C are all about 3.68. (e, f) The detailed contours corresponding to peaks A and B. The rotation angle of panels (d)–(f) is $\pi/6$.

for $x < 300$, where peaks A–C are due to the periodic systems with $c = 12\,545$, 3361, and 901, correspondingly, the periods are $\sqrt{12\,545/2}\pi$, $\sqrt{3361}\pi$, and $\sqrt{901}\pi$. These are in agreement with the analysis based on the Pythagoras triple. The periodic system due to peak A has the rotation angle $\arcsin(6273/12\,545) \approx 0.166\,68\pi$, an error of $10^{-5}\pi$ to the moiré angle $\pi/6$. This small Diophantine error results in a strongly localized wave packet, as observed from the figure.

Figures 7(e) and 7(f) illustrate the intersecting lines corresponding to peaks A and B in Fig. 7(d), where the black dashed lines are the projection lines of the periodic systems, slightly different from the projection line of the aperiodic system. In the enlarged subplots, the purple triangles represent the locations of these peaks, and the black circles are the corresponding peak locations of the periodic systems. Due to the periodic approximation, the black line crosses the central axis of the javelin-shaped domain. One can observe that, in each panel, the triangle and circle symbols are very close, demonstrating that the locations of wave packets for the aperiodic systems do have a relation to the approximate periodic systems. Let ε be the distance between the two symbols, representing the error in the locations of the wave packets. This error can be roughly estimated as $\varepsilon \approx T\Delta\theta$, where T is the period of the periodic system and $\Delta\theta$ is the difference between the twist angles of the aperiodic and periodic systems. ε values of peaks A–C are 0.0115, 0.0332, and 0.0427, respectively. $T\Delta\theta$ values are 0.0115, 0.0313, and 0.0428, which are high-precision approximations of ε. Hence, $T\Delta\theta$ can characterize the error in the localizations of the wave packets.

V. CONCLUSION

To summarize, we propose a highly efficient PI algorithm, which is a combination of the projection method and the indicator for aperiodic eigenproblems for photonic moiré lattices. The PI algorithm solves the problem directly without using periodic approximations such that the simultaneous Diophantine approximation can be avoided. It allows us to accurately calculate the band structure of the eigenstates in moiré lattices. In addition, we conduct analysis on connections between periodic and aperiodic systems in terms of their structures, numerical algorithms, and eigenstate properties. We find that the localized eigenstates in the moiré lattices are determined by the periodic lattices adjacent to it, leading to the Pythagoras superposition principle. This principle connects the relationship between the aperiodic and periodic lattices and is promising to further explore the moiré lattices and the wave-packet localization in 2D and 3D systems.

ACKNOWLEDGMENTS

Z.G. and Z.X. are supported by the National Natural Science Foundation of China (NNSFC) (Grant No. 12071288) and the Science and Technology Commission of Shanghai Municipality (Grants No. 20JC1414100 and No. 21JC1403700). Z.Y. is supported by the NNSFC (Grant No. 12101399) and the Shanghai Sailing Program (Grant No. 21YF1421000). F.Y. is supported by the NNSFC (Grant No. 91950120), Scientific Funding of Shanghai (Grant No. 9ZR1424400), and the Shanghai Outstanding Academic Leaders Plan (Grant No. 20XD1402000).

[1] R. Bistritzer and A. H. MacDonald, Proc. Natl. Acad. Sci. USA **108**, 12233 (2011).
[2] Y. Cao, V. Fatemi, S. Fang, K. Watanabe, T. Taniguchi, E. Kaxiras, and P. Jarillo-Herrero, Nature (London) **556**, 43 (2018).
[3] S. Carr, D. Massatt, S. Fang, P. Cazeaux, M. Luskin, and E. Kaxiras, Phys. Rev. B **95**, 075420 (2017).
[4] J. Gu, L. Ma, S. Liu, K. Watanabe, T. Taniguchi, J. C. Hone, J. Shan, and K. Mak, Nat. Phys. **18**, 395 (2022).
[5] C. Lau, M. W. Bockrath, M. Fai, and Z. Fan, Nature (London) **602**, 41 (2022).
[6] B. Han, D. Post, and P. Ifju, J. Strain Anal. Eng. Des. **36**, 101 (2001).
[7] A. González-Tudela and J. I. Cirac, Phys. Rev. A **100**, 053604 (2019).
[8] L. J. O'Riordan, A. C. White, and T. Busch, Phys. Rev. A **93**, 023609 (2016).
[9] G. Hu, A. Krasnok, Y. Mazor, C.-W. Qiu, and A. Alù, Nano Lett. **20**, 3217 (2020).
[10] X. Lu, P. Stepanov, W. Yang, M. Xie, M. A. Aamir, I. Das, C. Urgell, K. Watanabe, T. Taniguchi, G. Zhang, A. Bachtold, A. H. MacDonald, and D. K. Efetov, Nature (London) **574**, 653 (2019).
[11] B. Lou, N. Zhao, M. Minkov, C. Guo, M. Orenstein, and S. Fan, Phys. Rev. Lett. **126**, 136101 (2021).
[12] A. L. Sharpe, E. J. Fox, A. W. Barnard, J. Finney, K. Watanabe, T. Taniguchi, M. A. Kastner, and D. Goldhaber, Science **365**, 605 (2019).
[13] S. Fan and J. D. Joannopoulos, Phys. Rev. B **65**, 235112 (2002).
[14] J. M. B. Lopes dos Santos, N. M. R. Peres, and A. H. Castro Neto, Phys. Rev. Lett. **99**, 256802 (2007).
[15] S. Sinha, P. C. Adak, A. Chakraborty, K. Das, K. Debnath, L. V. Sangani, K. Watanabe, T. Taniguchi, U. V. Waghmare, A. Agarwal, and M. M. Deshmukh, Nat. Phys. **18**, 765 (2022).
[16] Y. Cao, V. Fatemi, A. Demir, S. Fang, S. Tomarken, L. Spencer, J. Y. Luo, J. D. Sanchez-Yamagishi, K. Watanabe, T. Taniguchi, E. Kaxiras, R. C. Ashoori, and P. Jarillo-Herrero, Nature (London) **556**, 80 (2018).
[17] E. Y. Andrei, D. K. Efetov, P. Jarillo-Herrero, A. H. MacDonald, K. F. Mak, T. Senthil, E. Tutuc, A. Yazdani, and A. F. Young, Nat. Rev. Mat. **6**, 201 (2021).
[18] L. Du, M. R. Molas, Z. Huang, G. Zhang, F. Wang, and Z. Sun, Science **379**, eadg0014 (2023).
[19] P. Wang, Y. Zheng, X. Chen, C. Huang, Y. V. Kartashov, L. Torner, V. V. Konotop, and F. Ye, Nature (London) **577**, 42 (2020).
[20] C. Huang, F. Ye, X. Chen, Y. V. Kartashov, V. V. Konotop, and L. Torner, Sci. Rep. **6**, 1 (2016).
[21] Y. Lahini, R. Pugatch, F. Pozzi, M. Sorel, R. Morandotti, N. Davidson, and Y. Silberberg, Phys. Rev. Lett. **103**, 013901 (2009).

[22] J. Billy, V. Josse, Z. Zuo, A. Bernard, B. Hambrecht, P. Lugan, D. Clément, L. Sanchez-Palencia, P. Bouyer, and A. Aspect, Nature (London) **453**, 891 (2008).
[23] A. L. Goldman and R. Kelton, Rev. Mod. Phys. **65**, 213 (1993).
[24] R. Lifshitz and D. M. Petrich, Phys. Rev. Lett. **79**, 1261 (1997).
[25] N. K. Efremidis, S. Sears, D. N. Christodoulides, J. W. Fleischer, and M. Segev, Phys. Rev. E **66**, 046602 (2002).
[26] J. Shen, T. Tang, and L.-L. Wang, *Spectral Methods: Algorithms, Analysis and Applications*, Springer Series in Computational Mathematics, Vol. 41 (Springer, Berlin, 2011).
[27] J. Zeng, Y. Hu, X. Zhang, S. Fu, H. Yin, Z. Li, and Z. Chen, Opt. Express **29**, 25388 (2021).
[28] H. Davenport and K. Mahler, Duke Math. J. **13**, 105 (1946).
[29] K. Jiang and P. Zhang, J. Comput. Phys. **256**, 428 (2014).
[30] J. Liesen and S. Zdenek, *Krylov Subspace Methods: Principles and Analysis* (Oxford University, Oxford, 2013).
[31] J. D. Joannopoulos, S. G. Johnson, J. N. Winn, and R. D. Meade, *Photonic Crystals: Molding the Flow of Light (second edition)* (Princeton University, Princeton, NJ, 2008).
[32] J. Liu, J. Sun, and T. Turner, J. Sci. Comput. **79**, 1814 (2019).
[33] R. Huang, J. Sun, and C. Yang, CSIAM Trans. Appl. Math. **1**, 463 (2020).
[34] T. Kato, *Perturbation Theory for Linear Operators, Classics in Mathematics*, Vol. 132 (Springer, Berlin, 2013).
[35] R. Huang, A. A. Struthers, J. Sun, and R. Zhang, J. Comput. Phys. **327**, 830 (2016).
[36] T. Schwartz, G. Bartal, S. Fishman, and M. Segev, Nature (London) **446**, 52 (2007).
[37] B. Freedman, G. Bartal, M. Segev, R. Lifshitz, D. N. Christodoulides, and J. W. Fleischer, Nature (London) **440**, 1166 (2006).
[38] L. Levi, M. Rechtsman, B. Freedman, T. Schwartz, O. Manela, and M. Segev, Science **332**, 1541 (2011).